Bichromatic synchronized chaos in driven coupled electro-optomechanical nanoresonators

Guilhem Madiot,[1] Franck Correia,[1] Sylvain Barbay,[1] and Rémy Braive[1,2]
[1]*Centre de Nanosciences et de Nanotechnologies, CNRS, Université Paris-Saclay, 91120 Palaiseau, France*
[2]*UFR de Physique, Université de Paris, F-75006 Paris, France*

(Received 17 May 2020; accepted 27 July 2021; published 27 August 2021)

Chaos and synchronization are important and ubiquitous phenomena in nature. Chaos synchronization spontaneously emerges in the collective dynamics of coupled nonlinear oscillators; however, its control remains a challenge at the nanoscale. Here, we present an experimental and theoretical investigation of synchronization on the route to chaos and in the chaotic regime in mechanically coupled electro-optomechanical nanocavities. In this system an integrated electroactuation enables one to drive the mechanical normal modes in the nonlinear regime while the mechanical displacement is transferred to an optical probe which provides a direct readout access to both their amplitude and phase responses. Using a single low-frequency modulation of the force applied to each normal mode, we induce a chaotic dynamics in the coupled nanoresonators. By applying a simultaneous force modulation on each of the normal modes, we generate chaos at two distinct carrier frequencies referred to as bichromatic chaos. The mode amplitudes are synchronized all the way on the route to chaos as well as in the chaotic regime. Meanwhile, their phases experience complex dynamics with imperfect synchronization in the chaotic regime. These results set the ground for applications of mechanical nanoresonators in areas such as metrology, multispectral chaotic encryption, and analog computing.

DOI: 10.1103/PhysRevA.104.023525

I. INTRODUCTION

Synchronization is a phenomenon commonly observed in macroscopic coupled or driven oscillating systems [1]. Since the work of Huygens [2], such phenomenon has been found in many fields of science, e.g., in physics [3–6], chemistry [7], biology [8], ecology [9], economy [10], and even in sociology [11]. Signatures of synchronization can be imprinted on the dynamics of both quadratures of the investigated signal, i.e., on the amplitude and the phase. However, the latter exhibits a much richer dynamics which may experience over time either periodic or erratically distributed jumps and many other regimes, as described in the Kuramoto model [7]. Even though synchronization of chaotic systems may seem counterintuitive [12], the investigation and implementation of such a phenomenon is particularly meaningful and has applications from large-scale systems in meteorology [13] to lasers [14] for, e.g., secure chaotically encrypted communications [15,16].

In the general case of nonidentical chaotic oscillators, complete synchronization of the amplitudes and phases is expected only for strongly coupled systems [17]. For smaller coupling strength, either phase locking or imperfect phase synchronization (IPS) [18] is observed. IPS corresponds to the case where intermittent phase slips occur while the amplitudes are generally not fully synchronized. This phenomenon has received a large theoretical interest [19–21] with few experimental demonstrations only at the macroscopic scale, in electronic circuits [22,23] or Nd:YAG lasers [24]. However, at the nanoscale—where the collective dynamics of large oscillators' arrays can be deeply studied—synchronization remains a challenge due to ineluctable fabrication disorder.

Large nonlinearities at the origin of chaotic dynamics can be achieved in nanoscale mechanical and optomechanical systems [25–30]. Thus, thanks to their experimental adaptability [5,25] and possibility of accurate modeling [31,32], it makes them a platform of choice to test and evidence these concepts. As such, we note that synchronization [33–35] and chaos [36,37] have been separately investigated in single or coupled nanoelectromechanical systems. In line with these latest studies, chaos with electro- or optomechanical systems has been extensively studied theoretically [38–41]. Only recently and using a single resonator, experimental demonstrations of chaos in an optomechanical cavity have been reported [42,43] with a strong optical driving.

Here we evidence IPS between optical signals at two distinct carrier frequencies. This is achieved with two mechanically coupled electro-optomechanical nanocavities. Chaos is first observed independently on each normal mode, using a low-frequency modulated monochromatic drive. This experiment evidences that the dynamics is transferred through spring coupling between the subsystems despite their intrinsic natural frequency mismatch. Moreover, through the optomechanical scheme, chaos is transferred from the mechanical to the optical domain. By simultaneously driving and modulating the normal modes at their respective frequency, a nonlinear reciprocal coupling occurs due to orthogonality breaking. Interestingly, the quadrature amplitudes of the two chaotic signals at two different tones are synchronized. Meanwhile the quadrature phases evidence different regimes from synchronous evolution in phase-locked regime to imperfect phase synchronization in chaotic regime. The bichromatic excitation allows synchronized chaos to be generated at two distinct carrier frequencies opening potential new avenues

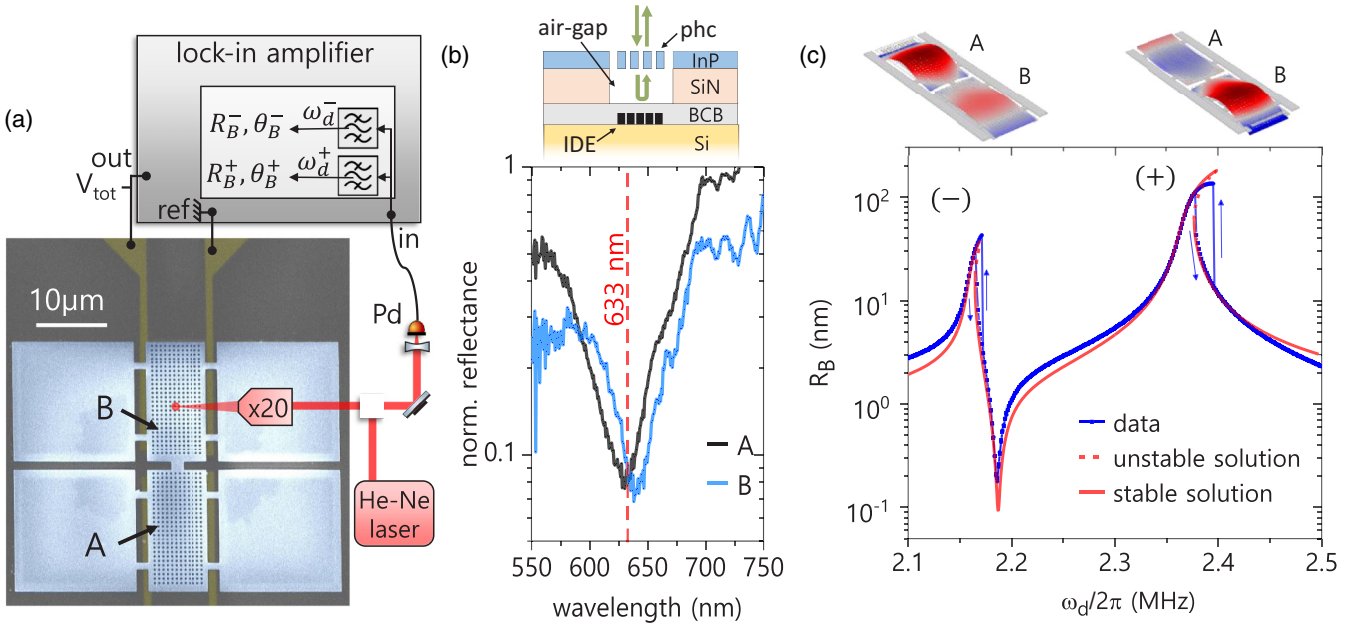

FIG. 1. (a) False color scanning electron microscope image of the two suspended membranes (A, B) bridged by a coupling nanobeam (blue). Gold stripes are visible underneath the membranes for electroactuation with IDEs (yellow). Schematic experimental setup with electrical actuation on the IDEs and optical readout. The response signal is demodulated with two bandpass filters respectively centered on the driving frequencies. (b) Reflectance spectra of the two Fabry-Pérot cavities formed by membranes A (black) and B (blue) and the substrate. Inset: Schematic of an injected cavity. (c) Mechanical displacement of membrane B under forward and backward sweeps of the driving frequency with excitations $V_{dc} = 2$ V and $V_{ac} = 3$ V (blue line) and fit (red lines) with the Duffing-Duffing model. Insets: Displacement field of each eigenmode simulated by the finite-element method.

to synchronized multifrequency data encryption [44–47] and random number generation [48].

The unequivocal description of these regimes is enabled by the measurement method which gives direct access to the dynamical variables, without making any use of reconstructed signals. These phenomena can be understood and fully supported by numerical simulations based on a classical model using Duffing resonators which, beyond nanomechanics, can be used in many fields including superconducting Josephson amplifier [49], ionization plasma [50], and complex spatiotemporal behaviors such as chimera sates [51].

II. EXPERIMENTAL SYSTEM AND DETECTION SCHEME

The experimental system [see Fig. 1(a)] consists of two coupled mechanical microresonators made of a 260-nm-thick InP layer suspended over a 380-nm air gap. Each membrane is a (10×20)-μm^2 rectangle pierced with a square lattice of cylindrical holes which allows an enhancement of the out-of-plane reflectivity [52]. The two membranes are mechanically coupled through a 1-μm-wide and 1.5-μm-long bridge. A pair of gold interdigitated electrodes (IDEs) is positioned on the substrate below each resonator and allows for independent actuation of the mechanical resonators. The fabrication process is described in Ref. [53]. All measurements are done at room temperature and the chip is placed in a vacuum chamber pumped below 10^{-5} mbar. The system composed of the membrane plus the IDEs constitutes a low-finesse optical cavity which we can probe for measuring the mechanical displacement [see inset in Fig. 1(b)]. The reflectance spectra shown in Fig. 1(b) are measured by focusing a supercontinuum laser on the centers of the at-rest membranes with a ×20 microscope objective. The resulting spectra are normalized with a reference measurement obtained by pointing the laser at an on-chip gold planar surface. For each membrane, the reflectance shows a pronounced dip typical of a Fabry-Pérot cavity resonance and centered around 630 nm with optical Q factors of about 10. In the following experiments, only the membrane B is probed. The reflectance dip matches with the helium-neon wavelength $\lambda = 633$ nm which is used in the following for the optical readout of the calibrated displacement of membrane B, R_B. This also ensures the transduction of the mechanical motion into the optical phase of the probe field. Thus the optical cavity is used as a passive optomechanical transducer enhancing the readout. It is assumed not to play a role in the dynamics of the system in the following.

We first apply a driving voltage $V_{tot} = V_{dc} + V_{ac}\cos(\omega_d t)$ where V_{dc} is a static voltage and V_{ac} is the amplitude of the ac driving at frequency ω_d. The electrocapacitive force exerted by the IDEs on membrane B reads [26]

$$F = \frac{1}{2}\frac{dC}{dx}V_{tot}^2, \tag{1}$$

where $C(x)$ is the position-dependent capacitance of the membrane/IDEs system. A calibration of the force gives $|dC/dx| = 2.2\ \mu N\,V^{-2}$. We access the mechanical modes of the system by sweeping the driving frequency while recording the response signal of membrane B. The latter is demodulated at the driving frequency via a 100-Hz-wide bandpass filter. This operation enables us to access both the amplitude of the

signal—that we convert into a displacement of membrane B, R_B—and its phase, θ_B. Calibrations of the displacement and of the driving force are detailed, respectively, in Appendices A and B. In the linear regime, at low amplitude driving, the fundamental normal modes of the coupled membranes are centered, respectively, at $\omega_- = 2\pi \times 2.163$ MHz and $\omega_+ = 2\pi \times 2.374$ MHz (see Aappendix C). Finite-elementmethod simulations allow one to identify the in-phase (−) and out-of-phase (+) modes with their respective displacement fields shown in the inset of Fig. 1(c). Importantly the natural frequency mismatch $\omega_B - \omega_A$ is quite significant and leads the normal mode (−) [respectively, (+)] to be dominated by the motion of membrane A (respectively, membrane B). This is also confirmed by measuring the impact of a change in one natural frequency on the normal mode frequencies (see Appendix D).

The mechanical response of the system in the nonlinear regime is shown in Fig. 1(c) for $V_{\rm dc} = 2$ V and $V_{\rm ac} = 3$ V. It displays two hysteretic regions around ω_- and ω_+ that are evidenced by sweeping ω_d forward and backward. The effective mode coupling is attested by the presence of a destructive interference dip which is typical of a Fano resonance [54–56] between the nearly identical resonators, as confirmed by the modelization. The observed bistable responses arise from intrinsic mechanical nonlinearities [57] which can be modeled thanks to a Duffing oscillator model [53,58].

In the case of coupled membranes, the model writes

$$\begin{aligned} &\ddot{x}_A + \Gamma_A \dot{x}_A + \omega_A^2 x_A + \beta x_A^3 - G x_B = 0, \\ &\ddot{x}_B + \Gamma_B \dot{x}_B + \omega_B^2 x_B + \beta x_B^3 - G x_A = F_B \cos \omega_d t, \end{aligned} \tag{2}$$

where $x_{A,B}$ are the mechanical displacements of membranes A and B, $\Gamma_{A,B}$ the membranes' mechanical dampings, β the Duffing nonlinearity, and G is the membrane coupling. The resonant frequencies of the mechanical resonators are $\omega_{A,B}$ and a near-resonant mass-normalized force F_B is acting on membrane B. A fit of the nonlinear response [Fig. 1(c)] allows one to retrieve the values of the physical parameters. We obtain the resonant frequencies $\omega_A = 2\pi \times 2.187$ MHz and $\omega_B = 2\pi \times 2.345$ MHz and the mechanical dampings $\Gamma_A = 2\pi \times 2.4$ kHz and $\Gamma_B = 2\pi \times 4.3$ kHz. The resonant frequencies mismatch arises because of fabrication imperfections. We extract the cubic nonlinearity $\beta = (2\pi)^2 \times 6.71 \times 10^{-6}$ MHz^2 nm^{-2}. The reduced coupling constant is obtained from a fit of the linear response (see appendix C) and is given by $G/\omega_A \approx 2\pi \times 130$ kHz.

In the context of identical resonators, the strong-coupling regime is established when the criterion $G/\omega_A > \Gamma_A$ is satisfied [59]. This criterion applies in our experiment; however, since the resonator frequency mismatch is about twice as large as the minimum normal mode splitting, we are rather in an intermediate regime between the strong- and weak-coupling cases.

III. CHAOTIC DYNAMICS WITH A MONOCHROMATIC EXCITATION

An additional low-frequency modulation signal is added to the total voltage applied to the membrane B set of IDEs. It now writes $V_{\rm tot} = V_{\rm dc} + V_{\rm ac}\cos(\omega_d t) + V_p \cos(\omega_p t)$ with V_p and $\omega_p \ll \omega_d$ the modulation amplitude and frequency, respectively. We reduce the set of experimental variables by locking $V_{\rm dc} = 2$ V and $V_{\rm ac} = 3$ V while V_p is used as the control parameter to explore the dynamical changes of the system. The modulation frequency is set to $\omega_p = 2\pi \times 7$ kHz. The driving frequency is set to the low-frequency edge of the (−) eigenmode bistability curve at $\omega_d = 2\pi \times 2.164$ MHz. The He-Ne laser is focused on membrane B and the modulation amplitude V_p is swept from 0 to 3 V. Higher values are not reached in order to preserve the mechanical system from failure. For each value of V_p, we record the signal quadratures $X_B = R_B \cos(\theta_B)$ and $Y_B = R_B \sin(\theta_B)$ in real- time thus accessing simultaneously phase and amplitude components. The signal is demodulated with a 40-kHz-wide bandpass filter centered at ω_d. The sampling rate is 500 kHz and each trace has a length of 100 ms, ensuring that several hundreds of modulation periods are recorded. The Poincaré section made of the local maxima of $Y_B(t)$ as a function of V_p is shown in Fig. 2(a). Using $Y_B(t)$ rather than $X_B(t)$ is an arbitrary choice motivated by the higher amplitude of the phase portraits along the Y axis. Additionally, each time trace is used to compute the largest Lyapunov exponent (LLE) shown below the diagram. We use the TISEAN package [60] routine implementing the Rosenstein algorithm [61]. For four positions on the diagram corresponding to a typical dynamical regime, we plot $Y_B(t)$ as a function of $X_B(t)$ in a phase portrait in Fig. 2(b). For a low value of the modulation voltage injected into the normal mode (−), the Poincaré section in Fig. 2(a) results in a closed single loop. In this limit-cycle oscillation regime the membrane oscillation envelope is modulated at ω_p. As the amplitude is modulated stronger, we observe two consecutive period-doubling bifurcations [62] at $V_p \approx 1.75$ V and $V_p \approx 2.5$ V prior to a window of chaotic dynamics for a modulation amplitude higher than 2.8 V. The presence of chaos is confirmed by the presence of a strictly positive LLE while it is zero for limit-cycle oscillations. Similar measurements are conducted driving the other normal mode (+). By setting the driving frequency to the low edge of the bistability at $\omega_d = 2\pi \times 2.379$ MHz, we now construct the bifurcation diagrams by reading the motion of membrane B [Fig. 2(d)]. The phase portraits associated to particular positions of this latter case are shown in Fig. 2(e). The bifurcation diagrams of eigenmode (+) also display a period-doubling route to chaos structure although the chaotic regime now occurs around $V_p \approx 2$ V. Most interestingly, we observe chaos intermittency (i.e., several chaotic regions that are separated by small windows of periodic or quasiperiodic regimes) as captured by the zero values of the associated LLE [see Fig. 2(e)]. Both experimental diagrams share a common dynamics but the bifurcation points significantly differ whether the eigenmode (−) or (+) is driven. These quantitative differences between the eigenmodes dynamics result from the imbalanced energy injection in the normal modes since only membrane B is driven.

The bifurcation diagram using the membrane B response for the mechanical mode (−) [respectively, for the mode (+)] is numerically reproduced in Fig. 2(c) [respectively, in Fig. 2(f)] using the Duffing-Duffing model developed previously at the driving frequency $\omega_d = 2\pi \times 2.167\,38$ MHz without any further adjustable parameter (respectively, at $\omega_d = 2\pi \times 2.37940$ MHz). The simulations

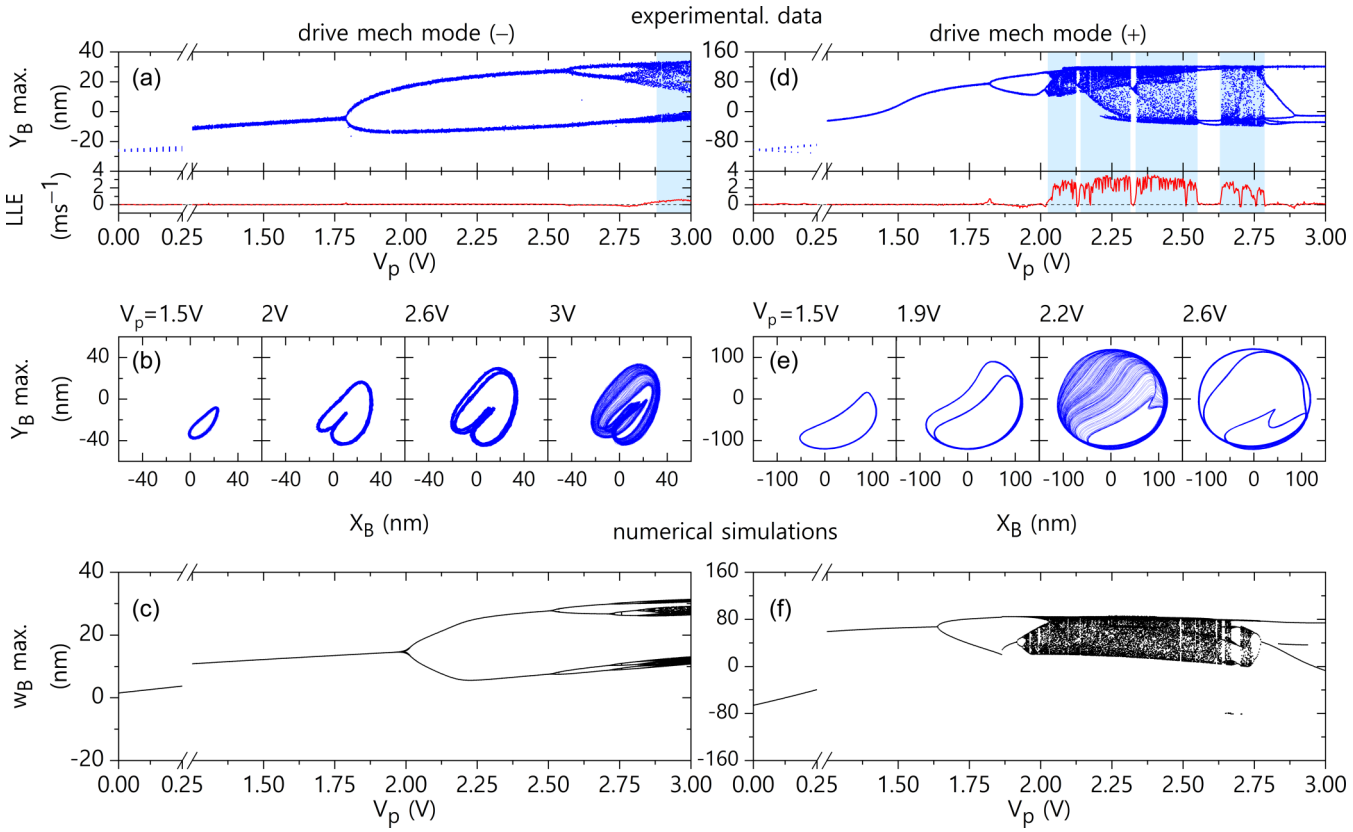

FIG. 2. (a)–(d) Experimental bifurcation diagrams built by sweeping V_p and reading membrane B. A modulated drive is applied, respectively, on the in-phase mode with $\omega_d = 2\pi \times 2.164$ MHz or on the out-of-phase mode with $\omega_d = 2\pi \times 2.379$ MHz. We use $V_{\rm dc} = 2$ V, $V_{\rm ac} = 3$ V, and $\omega_p = 2\pi \times 7$ kHz. The largest Lyapunov exponent (LLE) is shown below. Note the broken axis. (b)–(e) Phase portraits built from response of membrane B in different dynamical regimes. (c)–(f) Numerical bifurcation diagrams built by solving the dynamics of membrane B.

implement an adaptative step-size RK4 method to solve the reduced coupled-Duffing oscillators' equations, including a time-dependent forcing (see appendix E) and injecting the experimentally determined parameters. This results in a modulated force amplitude

$$F_B(t) \propto V_{\rm ac}[V_{\rm dc} + V_p \cos(\omega_p t)]. \tag{3}$$

Note that in the literature, similar perturbative approaches aiming to generate and control chaos in nonlinear oscillators also implement the Duffing model [63–66].

The simulated time traces are analyzed with the same protocol used for our experimental data. We use the quadrature w_B, which is the numerical equivalent of the observable Y_B. The route to chaos by period-doubling cascade is well captured by our model. The quantitative comparison with the experimental results yields a very satisfactory agreement. The period-doubling cascade bifurcation positions are corroborated with a continuation method. Additional experimental and numerical analysis further show that the modulation frequency plays a role in the appearance of the chaotic regime and a large window of frequencies around the damping timescale $\Gamma_{A,B}^{-1}$ leads to chaos.

Interestingly, the chaotic dynamics of the membranes is imprinted in the laser field intensity thanks to the integrated Fabry-Pérot cavity. This mechanical-to-optical chaos transfer is an interesting concept to exploit in chaos-based technologies. Furthermore, the transfer of the chaotic dynamics from one membrane to the other is possible in spite of the mismatch between the membranes natural frequencies. This allows one to simultaneously envision chaotic dynamics at distinct frequencies.

IV. IMPERFECT PHASE SYNCHRONIZATION UNDER BICHROMATIC EXCITATION

With a single tone drive, it is not possible to induce a sufficiently strong nonlinear response in both modes such that their responses synchronize. Therefore, we inject energy in both normal modes by using a bichromatic drive. Thus bidirectional nonlinear coupling of the normal modes is made possible thanks to the orthogonality breaking of these latter in the Duffing regime [67,68]. The new total voltage applied on the membrane B set of IDEs writes

$$V_{\rm tot} = V_{\rm dc} + V_{\rm ac}^- \cos(\omega_d^- t) + V_{\rm ac}^+ \cos(\omega_d^+ t) + V_p \cos(\omega_p t).$$

With $V_{\rm dc} = 2$ V, $V_{\rm ac}^- = 3.5$ V, $\omega_d^- = 2\pi \times 2.177$ MHz, $V_{\rm ac}^+ = 0.5$ V, $\omega_d^+ = 2\pi \times 2.410$ MHz, and $\omega_p = 2\pi \times 5$ kHz, the force exerted on membrane B thus has two components $F_B^- \cos(\omega_d^- t)$ and $F_B^+ \cos(\omega_d^+ t)$. We chose $V_{\rm ac}^+ < V_{\rm ac}^-$ in order to balance the normal mode response amplitudes. This way we also ensure that both modes display a chaotic dynamics. We use two independent demodulators to

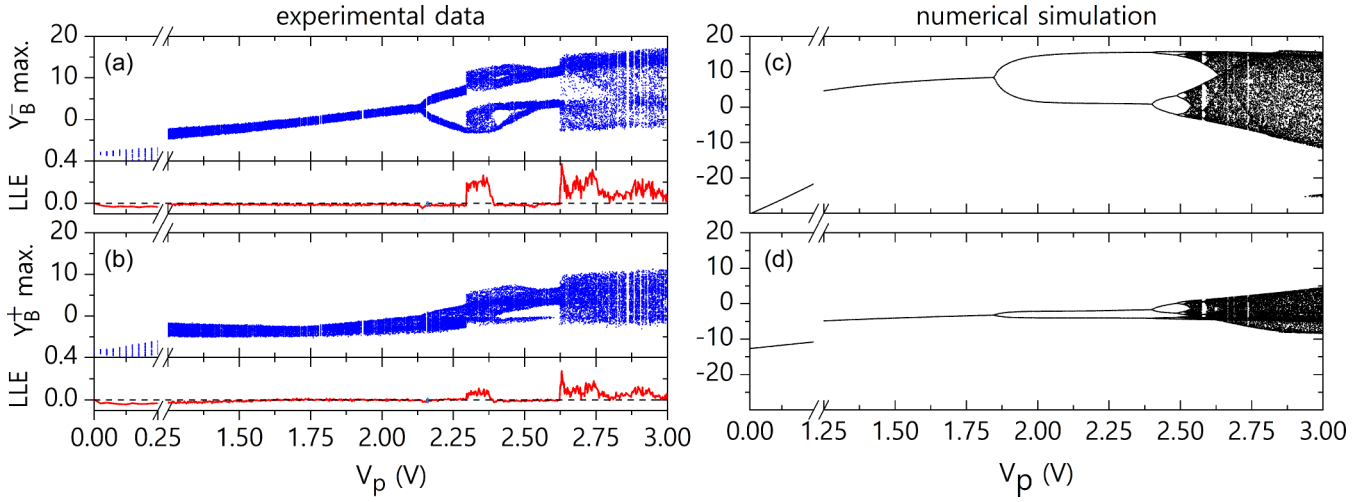

FIG. 3. (a), (b) Experimental bifurcation diagrams and associated calculated largest Lyapunov exponent (LLE in ms^{-1}) built from the normal modes response quadrature Y_B^- and Y_B^+ in units of nanometers with swept parameter V_p. The modes are driven at $V_{ac}^- = 3.5$ V and $V_{ac}^+ = 0.5$ V at frequencies $\omega_d^- = 2\pi \times 2.177$ MHz and $\omega_d^+ = 2\pi \times 2.410$ MHz with amplitude modulation at $\omega_p = 2\pi \times 5$ kHz. (c), (d) Simulated bifurcation diagrams based on the calibrated reduced model and using the driving frequencies $\omega_d^- = 2\pi \times 2.168\,500$ MHz and $\omega_d^+ = 2\pi \times 2.370\,280$ MHz.

simultaneously access the signal amplitude and phase at ω_d^- (R_B^- and θ_B^-) and at ω_d^+ (R_B^+ and θ_B^+). By sweeping the parameter V_p, two bifurcation diagrams are built, respectively, from the local maxima of signal quadratures $Y_B^- = R_B^- \sin(\theta_B^-)$ and $Y_B^+ = R_B^+ \sin(\theta_B^+)$ [see Figs. 3(a) and 3(b)]. Cross talks between the two demodulators are reduced by nearly −46 dB, by use of 40 kHz cut-frequency bandpass filters. We note that the diagram branches are broader than in the monochromatic experiment. This comes from the integration of noise and signal over a large spectral span. The qualitative comparison of the bifurcation diagrams shows a clear match of the dynamical regimes in which the normal modes (−) and (+) settle; more importantly, the bifurcation points are the same. After a limit-cycle region, both display an identical period-doubling route to chaos structure confirmed by the LLE. Numerical simulations of a reduced model (see appendix F) allow one to recover a similar bifurcation diagram as can be seen in Figs. 3(c) and 3(d).

To study the amplitude synchronization of the responses, we plot in Figs. 4(a)–4(c) (top row) $(R_B^\pm - \langle R_B^\pm \rangle)/\sigma^\pm$, the normalized response amplitudes for three identified dynamical regimes, with $\langle R_B^\pm \rangle$ and $\sigma^\pm$, respectively, the mean value and the standard deviation of $R_B^\pm(t)$ calculated over the entire time trace. The dashed black lines correspond to the synchronization regime where both normalized amplitudes are equal. Below the period-doubling bifurcation, for $V_p < V_{PD} = 2.140$ V, a master-slave relation is established between the drive and each resonance so these two inescapably move in synchrony. This corresponds to the phase-locked (PL) regime. For $V_p > V_{PD}$ the responses are now driven in a high-order synchronization regime. Nevertheless, the amplitudes are clearly correlated to each other. This is even more manifest in the chaotic regime where the amplitudes are still correlated despite their asynchronous phase behavior with the drive. This regime corresponds to the chaotic synchronization of the nonlinearly coupled normal modes. We now focus on the phase response correlations shown in Figs. 4(a)–4(c) (bottom row). In each case, we fit the data with a unit-slope line (black-dashed) corresponding to the synchronization regime $\frac{d}{dt}(\theta_B^+ - \theta_B^-) = 0$. These plots show a tendency of synchronous evolution of θ_B^- and θ_B^+ under force modulation for $V_p < V_{PD}$. Contrary to the amplitudes, the synchronization of the phases is not maintained for $V_p > V_{PD}$.

By studying the real-time dynamics of the phase difference [see Fig. 5], we find that 2π phase slips occur when $V_p > V_{PD}$ while the resonators evolve in synchrony in the PL regime for $V_p < V_{PD}$ (green trace). When high-order synchronization is established between each mode and the drive [1], phase slips resulting from phase desynchronization (PDS) can come

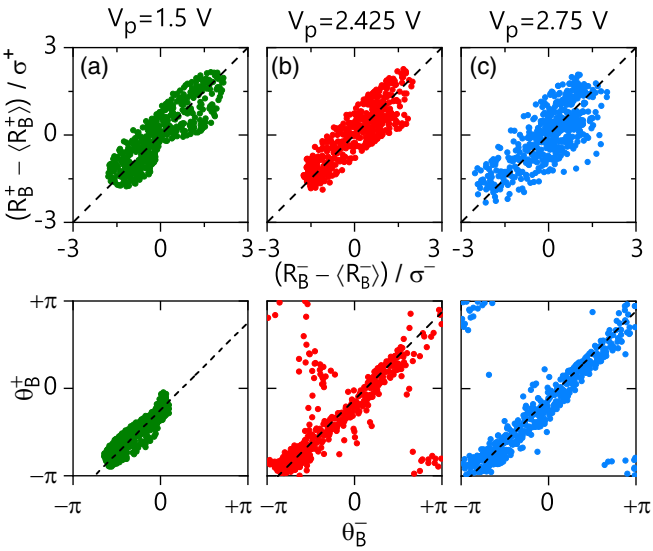

FIG. 4. For $V_p = 1.5$ V, $V_p = 2.425$ V, and $V_p = 2.75$ V: Experimental phase portraits showing the normal modes relative response normalized amplitudes (a) and phase (b) with perfect amplitude or phase synchronization references (black-dashed lines).

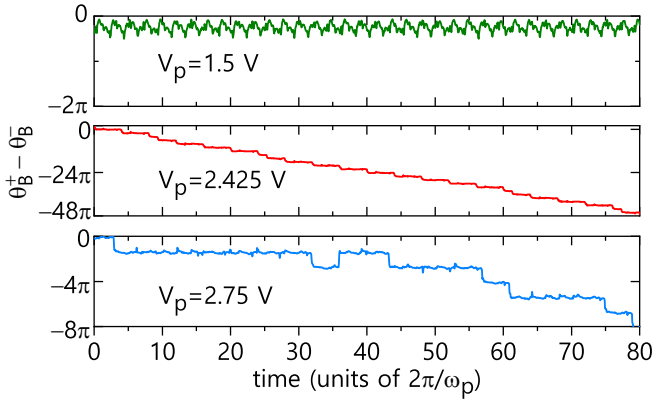

FIG. 5. Response phase difference $\theta_B^+ - \theta_B^-$ over 80 modulation periods (16 ms) for different V_p values: synchronous dynamics in phase-locked (PL) regime ($V_p = 1.5$ V, green), phase desynchronization (PDS) ($V_p = 2.425$ V, red), and imperfect phase synchronization (IPS) ($V_p = 2.75$ V, blue).

up even if the amplitudes stay correlated. This process leads to phase slips occurring regularly (red trace)—in this situation, the phases periodically execute one more (or one less) cycle regarding the drive—or chaotically (blue trace) with possibly long durations of phase-synchronized evolution. This corresponds to the imperfect phase synchronization (IPS) scenario [17].

The different synchronization regimes can be described through a statistical study of the durations between two successive phase slips. For a given time trace, we list all the phase synchronization (PS) durations τ and calculate both the mean value $\langle\tau\rangle$ as well as the standard deviation σ_τ. In Fig. 6(a), we plot the scaled mean PS duration $\langle\tau\rangle/\sigma_\tau$ as a function of

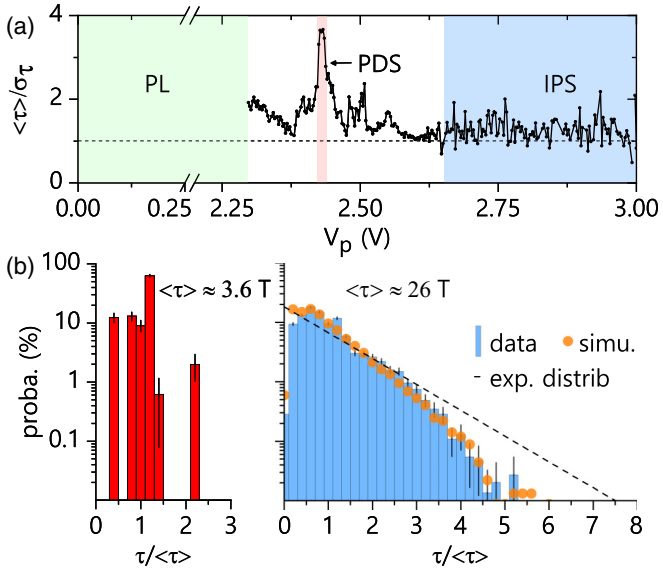

FIG. 6. (a) Scaled mean phase synchronization (PS) duration $\langle\tau\rangle/\sigma_\tau$ as a function of V_p. (b) Experimental probability distributions of the PS durations within the PDS (red) or the IPS (blue) regimes. Numerical distribution in the chaotic regime (orange dots) and exponential distribution (black dashed) are shown for comparison.

V_p. No value can be estimated below the bifurcation to chaotic regime at $V_p = 2.3$ V since the PL regime is established and therefore we do not observe any phase slip in the data. The PDS regime around $V_p = 2.425$ V is identified by the regularity of the phase slips with a small standard deviation of the PS durations leading to a peak in the scaled mean PS duration. As this peak is found precisely on a bifurcation point separating a period-4 motion from chaos, PDS might result here from particularly unstable phase dynamics at this position. In order to compare the statistics of τ between the different traces obtained for different V_p, we normalize all the synchronized phase durations found in a given trace by the mean duration value for this trace. In the PDS regime [red stripe in Fig. 6(a)], the probability distribution is concentrated around 1, meaning that most of the durations are near the mean value $\langle\tau\rangle = 3.6$ modulation periods.

Note that the histogram displays a 63% probability for the phases to synchronize during four modulation periods because this PDS occurs while the system sets in a period-4 motion dynamics. In the chaotic regime [blue stripe in Fig. 6(a)], we find that the scaled mean PS duration remains constant and slightly over 1, which tends to indicate an almost exponential probability distribution [Fig. 6(b) (right)]. In this regime the mean PS duration is $\langle\tau\rangle = 26$ modulation periods. The probability distribution indeed decays exponentially but we find that the probability around the mean PS duration ($\tau/\langle\tau\rangle = 1$) is significantly higher than predicted with this distribution. Additionally, the observed long PS duration occurrences are more unlikely. We conclude that the phase slips constitute a non-Poissonian process due to the deterministic chaotic dynamics and do not result from noise. Relying on the simulated diagrams in Figs. 3(c) and 3(d), we also reproduce a histogram of the PS durations in Fig. 6(b) integrated over a range of modulation amplitude showing a chaotic domain. We find a good agreement with the experimental distribution.

Even though a natural frequency mismatch of nearly 10% is observed in our system, synchronized dynamics is observed. This highlights the robustness of such phenomenon with regard to the frequency mismatch highly inherent to nanofabricated resonators. However, one should expect that higher disorder becomes a major limitation for one to address both normal modes via one subsystem with reasonable drive powers.

Further numerical adjustments of the two driving frequencies in a restricted range evidence the possibility to achieve perfect phase (and amplitude) synchronization in the chaotic regime. This could be of major interest for applications based on chaos such as synchronized random number at two distinct carrier frequencies.

V. CONCLUSION

Beyond the chaotic behavior of a single resonator, we have deeply investigated and analyzed the chaotic and synchronization dynamics of distinct mechanically coupled electro-optomechanical nanoscale resonators based on two slowly modulated near-resonant drives. Chaos is first observed independently on each normal mode, using a low-frequency modulated monochromatic drive. The experimentally built bifurcation diagrams, with a direct measurement of all the

dynamical variables, are numerically reproduced using a calibrated model of coupled nonidentical Duffing oscillators. Chaos transfer on different carrier frequencies from MHz in mechanics to THz in optics is undoubtedly opening more avenues for random number generation based on optomechanics and more schemes for data encryption, chaotic optomechanical sensing, optomechanical logic, and chaos computing. By simultaneously driving and modulating the normal modes at their respective frequency, a nonlinear reciprocal coupling occurs due to orthogonality breaking. Interestingly, the quadrature amplitudes of the two chaotic signals at two different tones are synchronized. Meanwhile the phases evidence different regimes from synchronous evolution in phase-locked regime to imperfect phase synchronization in chaotic regime. Statistical study of the synchronization durations results in nonexponential distribution confirmed by our theoretical description attesting to the deterministic nature of the dynamics. Beyond low mechanical frequency carrier and thus low-frequency modulation, optomechanical crystals and their GHz frequencies could allow synchronization regimes for multispectral communications, where signals with different frequencies must carry the same encoded sequence and be a playground for integrated multispectral optomechanical communications at a frequency relevant for applications.

ACKNOWLEDGMENTS

This work is supported by the French RENATECH network, the European Union's Horizon 2020 research innovation program under grant agreement No. 732894 (FET Proactive HOT), the Agence Nationale de la Recherche as part of the "Investissements d'Avenir" program (Labex NanoSaclay, ANR-10-LABX-0035) with the flagship project CONDOR and the JCJC project ADOR (ANR-19-CE24-0011-01). We would like to acknowledge Marcel Clerc for fruitful discussions.

APPENDIX A: DISPLACEMENT CALIBRATION

The mechanical displacement R_B of membrane B converts to a measured voltage ηR_B with the conversion constant η, which can be extracted thanks to a Michelson interferometer. For that purpose, an opened-loop local oscillator is used, whose optical path difference with the sample arm is set to $\ell = \lambda/4$. Then the resonant oscillations amplitude of membrane B induced by a given driving strength, which translates to a voltage variation δV, is compared to the interferometric signal variation resulting from a small calibrated displacement $\delta\ell$ of the path difference. Doing this measurement for several excitation stages allows a confident estimation of the displacement calibration. We estimate the transduction constant to be $\eta \approx 0.5\ \mathrm{mV\,nm^{-1}}$.

APPENDIX B: FORCE CALIBRATION

We calibrate the electrocapacitive force applied on membrane B using

$$F = \frac{1}{2}\frac{dC}{dx}V_{\mathrm{tot}}^2. \tag{B1}$$

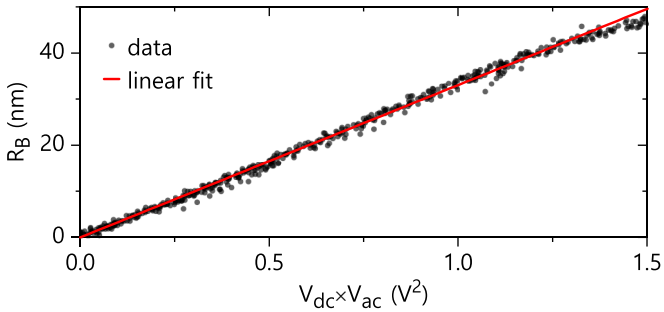

FIG. 7. Membrane B resonant response ($\omega_d = \omega_+ = 2.375$ MHz) amplitude measured as a function of the product $V_{\mathrm{dc}}V_{\mathrm{ac}}$. The data (black dots) are fitted with a line (red).

When expanded, this expression includes a static component $\propto (V_{\mathrm{dc}}^2 + V_{\mathrm{ac}}^2/2)$ that displaces the resonator by a negligible offset plus an off-resonant term at frequency $2\omega_d$, which is ignored in our model. A measurement of the displacement amplitude at demodulation frequency $2\omega_d$ indeed reveals an amplitude response less than 3% of that of the driven mode amplitude at ω_d. Therefore we conclude that the mass-normalized force amplitude exerted on membrane B can be simplified to its resonant contribution:

$$F_B = \frac{1}{m_{\mathrm{eff}}}\left|\frac{dC}{dx}V_{\mathrm{dc}}V_{\mathrm{ac}}\right|. \tag{B2}$$

The resonant displacement $R_B(\omega_d = \omega_+)$ is measured as a function of the product $V_{\mathrm{dc}}V_{\mathrm{ac}}$ (see Fig. 7). Given the strong natural frequency mismatch between the resonators, we assume a single resonator model for this calibration. In this case, the resonant response is given by

$$R_B(\omega_d = \omega_+) \approx \frac{F_B}{\Gamma_+\omega_+}, \tag{B3}$$

where $\Gamma_+ = 2\pi \times 1.9$ kHz is the damping rate of normal mode (+) and $m_{\mathrm{eff}} = 186$ pg its effective mass calculated with finite-element methods. We fit the data shown in Fig. 7 with a red line. The slope is found to be about $33\ \mathrm{nm\,V^{-2}}$ and Eq. (B3) directly gives the electrocapacitive force calibration $|\frac{dC}{dx}| = 2.2\ \mu\mathrm{N\,V^{-2}}$. The agreement is satisfying, and the discrepancy found both in the amplitude and in the phase around 2.2 MHz results from a mechanical displacement below the experimental sensitivity.

APPENDIX C: LINEAR RESPONSE FIT

We measure the mechanical response of membrane B while exciting the system with low voltages $V_{\mathrm{dc}} = 0.2$ V and $V_{\mathrm{ac}} = 1$ V. The response amplitude R_B and phase θ_B are recorded while the driving frequency is swept between 2.1 and 2.5 MHz, as shown in Fig. 8 (blue dots).

The stationary solutions derived from Eq. (2) of the main text can be easily obtained in the linear regime by setting the Duffing nonlinearity to 0 ($\beta = 0$). In this case, one can derive a complex expression for the displacement of membrane B:

$$\underline{r_B} = \frac{[2(\omega_d - \omega_A) - j\Gamma_A]F_B}{G^2 - [2(\omega_d - \omega_A) - j\Gamma_A][2(\omega_d - \omega_B) - j\gamma_B]}. \tag{C1}$$

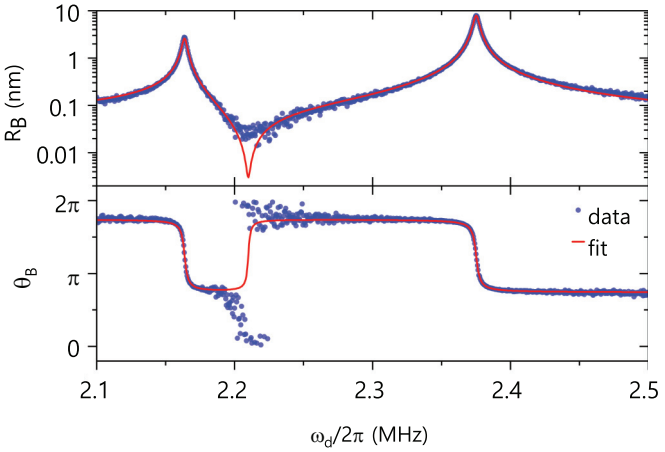

FIG. 8. Linear amplitude response (top) and phase response (bottom) of the system under excitation applied on membrane B with $V_{dc} = 0.2$ V and $V_{ac} = 1$ V. The data (blue) are fitted with the stationary solutions of two coupled linear-driven harmonic oscillators.

We use this expression to fit the data, with the amplitude and the phase respectively given by $r_B = \text{abs}(\underline{r_B})$ and $\theta_B = \arg(\underline{r_B})$. We fit simultaneously the amplitude and the phase, implying that only one set of parameters is returned, namely, the natural frequencies $\omega_{A,B}$, dampings $\Gamma_{A,B}$, and the coupling G. The force amplitude F_B is carefully calibrated in the next section. The resulting fit is shown with red lines in Fig. 8. The agreement is satisfying, and the discrepancy found both in the amplitude and in the phase around 2.2 MHz results from a mechanical displacement below the experimental sensitivity. We find $\omega_A = 2\pi \times 2.187$ MHz, $\omega_B = 2\pi \times 2.345$ MHz, $\Gamma_A \approx \Gamma_B = 2\pi \times 2.4$ kHz, and $G = (2\pi)^2 \times 0.284$ MHz^2.

APPENDIX D: MECHANICAL MODE IDENTIFICATION

After successfully fitting the membrane B response with a model of coupled harmonic oscillators (see previous section), we can conclude that the observed eigenmodes frequency difference is essentially caused by the natural frequency mismatch $\omega_B - \omega_A \approx 2\pi \times 158$ kHz. This implies that the eigenmodes $(-)$ and $(+)$ are respectively dominated by the motion of resonators A and B. In order the verify this conclusion, we apply a static voltage to the membrane B up to 25 V and observe how the eigenfrequencies are affected. It is well known that a static voltage acts on a micromechanical resonator as an additional residual stress [69]. This effect can be used to tune the frequency of an oscillator and demonstrate strong coupling between several resonators through the observation of an avoided crossing in the mechanical spectrum. We obtain the eigenfrequencies position by sweeping the drive frequency and measuring the response spectrum. A drive amplitude such that $V_{ac} < 0.1$ V is set to ensure a linear response and avoid possible confusion with any effect of the Duffing nonlinearity. The frequency displacements we observe [Fig. 9(a)] are not large enough to observe an avoided crossing. We compare the frequency displacements $\delta\omega_\pm = \omega_\pm(V_{dc}) - \omega_\pm(V_{dc} = 0)$ in Fig. 9(b) and it appears clearly that the eigenmode $(+)$ is mostly affected by the applied static voltage. In order to fit the data, we use the Jacobian defined

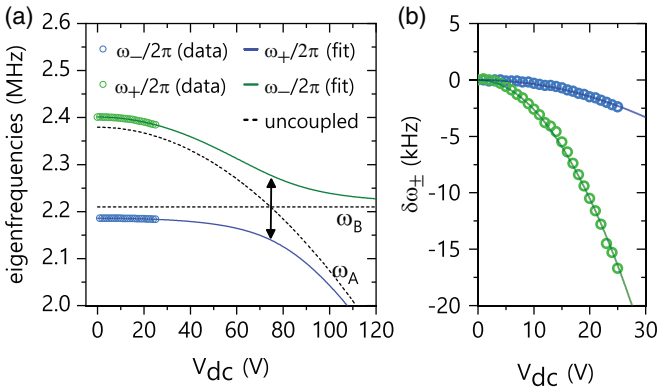

FIG. 9. (a) Measurement of the eigenfrequencies under static voltage V_{dc} applied on membrane B (symbols). The fit considers a parabolic shift of the self-coupled frequency ω_B (black dashed) that we use to solve the eigenmodes $(-)$ and $(+)$ (respectively, blue and green lines) resulting from the previously measured coupling G. An avoided crossing is predicted at $V_{dc} = 74$ V when the natural frequencies are equal (at arrow position). (b) Identical experimental data presented in terms of frequencies displacement $\delta\omega_\pm = \omega_\pm(V_{dc}) - \omega_\pm(V_{dc} = 0)$.

using the vector $(x_A, x_B, \dot{x_A}, \dot{x_B})$ and considering the coupled linear equations (2) (using $\beta = 0$):

$$J = \begin{pmatrix} 0 & 0 & 1 & 0 \\ 0 & 0 & 0 & 1 \\ -\omega_A^2 & G & -\Gamma_A & 0 \\ G & -\omega_B^2 & 0 & -\Gamma_B \end{pmatrix}.$$

The eigenvalues of J have imaginary parts that correspond to the normal modes' frequencies, which can be approximated to $\omega_\pm^2 \approx \frac{\omega_A^2+\omega_B^2}{2} \pm \sqrt{(\omega_A^2 - \omega_B^2)^2 + 4G^2}$, while their real parts correspond to the eigenmodes damping rates. We input the V_{dc}-dependent self-coupled frequency $\omega_B(V_{dc}) = \omega_B(0) + \alpha V_{dc}^2$. We assume the coupling $G/\omega_B \approx 2\pi \times 130$ kHz and use the unchanged self-coupled frequency $\omega_B(0)$ and the coefficient α as the fitting parameters. We find with this second method the frequency mismatch to be $\omega_B(0) - \omega_A(0) \approx 2\pi \times 168$ kHz, which confirms our first result. The resulting eigenmodes are shown with colored lines and the self-coupled frequencies with black-dashed lines in Fig. 9(a). It appears that $\omega_A \approx \omega_-$ and $\omega_B \approx \omega_+$ in the range of V_{dc} experimentally checked. The avoided crossing is predicted when the natural frequencies are equal, i.e., around $V_{dc} = 74$ V, which is out of reach in our experiment. Note that the assumption on the coupling value is only necessary to represent the level repulsion one would obtain with this voltage but does not affect our conclusion that the eigenmodes $(-)$ and $(+)$ are respectively dominated by the motions of membranes A and B.

APPENDIX E: DUFFING-DUFFING MODEL

This Appendix describes the derivations of the Duffing-Duffing model. We start with the master coupled equations describing two resonators A and B with respective displacements x_A and x_B, self-coupled frequencies ω_A and ω_B, damping rates Γ_A and Γ_B, and with identical Duffing cubic nonlinearity β. The resonators are coupled with the spring

coupling G. In agreement with the experiments, only the resonator B is externally driven:

$$\ddot{x_A} + \Gamma_A \dot{x_A} + \omega_A^2 x_A + \beta x_A^3 - G x_B = 0,$$
$$\ddot{x_B} + \Gamma_B \dot{x_B} + \omega_B^2 x_B + \beta x_B^3 - G x_A = F_B \cos(\omega_d t).$$

We take the ansatz $x_A = v_A \cos(\omega_d t) + w_A \sin(\omega_d t)$ and $x_B = v_B \cos(\omega_d t) + w_B \sin(\omega_d t)$ where the quadratures relate to the response amplitude and phase with $r_A^2 = v_A^2 + w_A^2$ and $\theta_A = \text{atan2}(w_A, v_A)$ (and similarly for r_B and θ_B). Before injecting the ansatz into the master equations, we find it useful to preliminarily calculate x_A^3 in order to reveal the off-resonant terms oscillating at $3\omega_d$ that we can neglect in the following. We also expand the expression for the derivatives $\dot{x}_A$ and $\ddot{x}_A$. We neglect the quadratures second derivatives by assuming $\ddot{v}_A, \ddot{w}_A \ll \omega_d^2 v_A, \omega_d^2 w_A$.

We now inject these preliminary results into the master equations. We use the normalized quantities $\omega_d t \to \tau$, $(\omega_B - \omega_d)/\omega_d \to \delta$, $(\omega_B - \omega_A)/\omega_d \to \Delta\omega$, $\Gamma_{A,B}/\omega_d \to \gamma_{A,B}$, $G/\omega_d^2 \to g$, $F_B/\omega_d^2 \to f_B$, and $\beta/\omega_d^2 \to \tilde{\beta}$. Note that $\omega_B^2 - \omega_d^2 \approx \omega_d^2 \delta$ and $\omega_A^2 - \omega_d^2 \approx 2\omega_d^2(\delta - \Delta\omega)$. It writes

$$\dot{v}_A = \tfrac{1}{2} w_A \big[2(\delta - \Delta\omega) + \tfrac{3}{4}\tilde{\beta}\big(v_A^2 + w_A^2\big)\big] - \tfrac{1}{2}\gamma_A v_A - \tfrac{1}{2} g w_B, \quad \text{(S.1.1)}$$

$$\dot{w}_A = \tfrac{-1}{2} v_A \big[2(\delta - \Delta\omega) + \tfrac{3}{4}\tilde{\beta}\big(v_A^2 + w_A^2\big)\big] - \tfrac{1}{2}\gamma_A w_A + \tfrac{1}{2} g v_B, \quad \text{(S.1.2)}$$

$$\dot{v}_B = \tfrac{1}{2} w_B \big[2\delta + \tfrac{3}{4}\tilde{\beta}\big(v_B^2 + w_B^2\big)\big] - \tfrac{1}{2}\gamma_B v_B - \tfrac{1}{2} g w_A, \quad \text{(S.2.1)}$$

$$\dot{w}_B = \tfrac{-1}{2} v_B \big[2\delta + \tfrac{3}{4}\tilde{\beta}\big(v_B^2 + w_B^2\big)\big] - \tfrac{1}{2}\gamma_B w_B + \tfrac{1}{2} g v_A + \tfrac{1}{2} f_B. \quad \text{(S.2.2)}$$

This system of equations describes the evolution of our system in terms of quadratures v_A, w_A, v_B, and w_B. It presents an interest for the numerical simulations since these quantities are homogeneous. However, we can obtain the final set of equations [Eq. (E1)] expressed in terms of the amplitudes and phases by performing the reverse transformations $v_A = r_A \cos(\theta_A)$, $w_A = r_A \sin(\theta_A)$, $v_B = r_B \cos(\theta_B)$, and $w_B = r_B \sin(\theta_B)$ and taking

$$\text{S.1.1} \times \cos(\theta_A) + \text{S.2.1} \times \sin(\theta_A),$$
$$\text{S.1.2} \times \cos(\theta_B) + \text{S.2.2} \times \sin(\theta_B),$$
$$-\text{S.1.1} \times \sin(\theta_A) + \text{S.2.1} \times \cos(\theta_A),$$
$$-\text{S.1.2} \times \sin(\theta_B) + \text{S.2.2} \times \cos(\theta_B).$$

The stationary solutions for the resonator amplitudes r_A and r_B and phases θ_A and θ_B can be described by the following set of equations:

$$\dot{r}_A = \frac{-\gamma_A}{2} r_A + \frac{g}{2} r_B \sin(\theta_A - \theta_B),$$
$$\dot{r}_B = \frac{-\gamma_B}{2} r_B - \frac{g}{2} r_A \sin(\theta_A - \theta_B) + \frac{f_B}{2}\sin(\theta_B),$$
$$r_A \dot{\theta}_A = \frac{-r_A}{2}\left[2(\delta - \Delta\omega) + \frac{3}{4}\tilde{\beta} r_A^2\right] + \frac{g}{2} r_B \cos(\theta_A - \theta_B),$$
$$r_B \dot{\theta}_B = \frac{-r_B}{2}\left[2\delta + \frac{3}{4}\tilde{\beta} r_B^2\right] + \frac{g}{2} r_A \cos(\theta_A - \theta_B) + \frac{f_B}{2}\cos(\theta_B). \quad \text{(E1)}$$

By assuming the permanent regime $\dot{r}_A = \dot{r}_B = \dot{\theta}_A = \dot{\theta}_B = 0$, the frequency domain response amplitude r_B is numerically solved using the experimental parameters. We adjust the solution on the experimental data by fitting with the remaining free parameter β and extract $\beta = (2\pi)^2 \times 6.71 \times 10^{-6}\ \text{MHz}^2\,\text{nm}^{-2}$.

The numerical simulations enabling one to reproduce the observed bifurcation diagrams integrate the equations (S.1.1), (S.1.2), (S.2.1), and (S.2.2) but including a time-dependent forcing:

$$\tilde{f_B}(t) = f_B\left(1 + \frac{V_p}{V_{\text{dc}}}\cos\omega_p t\right). \quad \text{(E2)}$$

APPENDIX F: BICHROMATIC DRIVE MODEL AND ORTHOGONALITY BREAKING

Driving both normal modes at the same time allows one to evidence synchronization phenomena. We model the system with the same master equation but add a second resonant excitation:

$$\ddot{x}_A + \Gamma_A \dot{x}_A + \omega_A^2\big(1 + \tilde{\beta} x_A^2\big) x_A - G x_B = 0,$$
$$\ddot{x}_B + \Gamma_B \dot{x}_B + \omega_B^2\big(1 + \tilde{\beta} x_B^2\big) x_B - G x_A = F_B^- \cos(\omega_d^- t) + F_B^+ \cos(\omega_d^+ t).$$

Since the system is now expected to respond both at ω_d^- and ω_d^+, we modify the ansatz:

$$x_A = v_A^- \cos(\omega_d^- t) + w_A^- \sin(\omega_d^- t) + v_A^+ \cos(\omega_d^+ t) + w_A^+ (\omega_d^+ t).$$

The rest of the calculations are essentially the same, except for the development of the cubic terms x_A^3 and x_B^3 where the nonlinear coupling between $r_{A,B}^-$ and $r_{A,B}^+$ comes from. We neglect all off-resonant terms including the ones oscillating at $2\omega_d^\pm - \omega_d^\mp$. Following the exact same procedure as before, we derive a system of eight coupled nonlinear ordinary differential equations for the normal modes $(-)$ and $(+)$ quadratures accessed either through membrane A (v_A^-, w_A^-, v_A^+, w_A^+) or membrane B (v_B^-, w_B^-, v_B^+, w_B^+). It writes

$$\dot{v}_A^\pm = \tfrac{1}{2} w_A^\pm \big[2\varepsilon_\pm(\delta_\pm - \Delta\omega) + \tfrac{3}{4}\varepsilon_\pm^2 \tilde{\beta}\big(r_A^{\pm^2} + 2 r_A^{\mp^2}\big)\big] - \tfrac{1}{2}\varepsilon_\pm \gamma_A v_A^\pm - \tfrac{1}{2}\varepsilon_\pm^2 g w_B^\pm,$$
$$\dot{w}_A^\pm = \tfrac{-1}{2} v_A^\pm \big[2\varepsilon_\pm(\delta_\pm - \Delta\omega) + \tfrac{3}{4}\varepsilon_\pm^2 \tilde{\beta}\big(r_A^{\pm^2} + 2 r_A^{\mp^2}\big)\big] - \tfrac{1}{2}\varepsilon_\pm \gamma_A w_A^\pm + \tfrac{1}{2}\varepsilon_\pm^2 g v_B^\pm,$$
$$\dot{v}_B^\pm = \tfrac{1}{2} w_B^\pm \big[2\delta_\pm + \tfrac{3}{4}\varepsilon_\pm^2 \tilde{\beta}\big(r_B^{\pm^2} + 2 r_B^{\mp^2}\big)\big] - \tfrac{1}{2}\varepsilon_\pm \gamma_B v_B^\pm - \tfrac{1}{2}\varepsilon_\pm^2 g w_A^\pm,$$
$$\dot{w}_B^\pm = \tfrac{-1}{2} v_B^\pm \big[2\delta_\pm + \tfrac{3}{4}\varepsilon_\pm^2 \tilde{\beta}\big(r_B^{\pm^2} + 2 r_B^{\mp^2}\big)\big] - \tfrac{1}{2}\varepsilon_\pm \gamma_B w_B^\pm + \tfrac{1}{2}\varepsilon_\pm^2 g v_A^\pm + \varepsilon_\pm \tfrac{1}{2} f_B^\pm,$$

where we use the amplitudes $r_A^{\pm^2} = v_A^{\pm^2} + w_A^{\pm^2}$ and $r_B^{\pm^2} = v_B^{\pm^2} + w_B^{\pm^2}$ for the compactness of these expressions. The parameter $\varepsilon_\pm = \omega_d^+/\omega_d^\pm$ aims to regularize the normalization of the parameters such that the time is arbitrarily chosen to be rescaled with $\omega_d^+ t$. Thus all the physical parameters are normalized consequently to this choice: $\delta_\pm = (\omega_B - \omega_d^\pm)/\omega_d^+$, $\Delta\omega = (\omega_B - \omega_A)/\omega_d^+$, $\gamma_{A,B} = \Gamma_{A,B}/\omega_d^+$, $g =$

$G/\omega_d^{+^2}$, $\tilde{\beta} = \beta/\omega_d^{+^2}$, and $f_B^{\pm} = f_B^{\pm}/\omega_d^{+}$. These two systems of four equations contain new terms that allow the normal mode response amplitudes $r_{A,B}^{+}$ and $r_{A,B}^{-}$ to couple. By expressing these equations in terms of amplitudes ($r_{A,B}^{\pm}$) and phases ($\theta_{A,B}^{\pm}$), the normal mode coupling takes the form $\tilde{\beta} r^{\pm} r^{\mp^2}$.

We integrate these equations using the parameters $V_{\mathrm{dc}} = 2$ V, $V_{\mathrm{ac}}^{-} = 3.5$ V, $V_{\mathrm{ac}}^{+} = 0.5$ V, $\omega_d^{-} = 2\pi \times 2.168\,500$ MHz, $\omega_d^{+} = 2\pi \times 2.370\,280$ MHz, and $\omega_p = 2\pi \times 5$ kHz. By sweeping V_p, a bifurcation diagram is reproduced with the amplitude response of both normal modes using the maxima of w_B^{-} and w_B^{+} [see Figs. 2(a) and 2(b) in the main text]. The phases θ_B^{-} and θ_B^{+} are both shifted by 100°, thus compensating an experimental dephasing. We analyze 1000 chaotic traces between $V_p = 2.742$ V and $V_p = 3$ V and extract more than 22 000 phase slip occurrences on which the statistical study of the phase synchronization durations is performed [see Fig. 5 in the main text].

[1] A. Pikovsky, M. G. Rosenblum, and J. Kurths, *Synchronization, A Universal Concept in Nonlinear Sciences* (Cambridge University Press, Cambridge, 2001).

[2] C. Huygens, *La Haye* (Société Hollandaise des Sciences, 1893), Vol. V.

[3] M. G. Rosenblum, A. S. Pikovsky, and J. Kurths, Phase synchronization in driven and coupled chaotic oscillators, IEEE Trans. Circuits Syst. I **44**, 874 (1997).

[4] A. N. Pisarchik and R. Jaimes-Reátegui, Intermittent lag synchronization in a driven system of coupled oscillators, Pramana **64**, 503 (2005).

[5] M. Zhang, G. S. Wiederhecker, S. Manipatruni, A. Barnard, P. McEuen, and M. Lipson, Synchronization of Micromechanical Oscillators Using Light, Phys. Rev. Lett. **109**, 233906 (2012).

[6] M. Zhang, S. Shah, J. Cardenas, and M. Lipson, Synchronization and Phase Noise Reduction in Micromechanical Oscillator Arrays Coupled through Light, Phys. Rev. Lett. **115**, 163902 (2015).

[7] Y. Kuramoto and T. Yamada, Pattern formation in oscillatory chemical reactions, Prog. Theor. Phys. **56**, 724 (1976).

[8] L. Glass, Synchronization and rhythmic processes in physiology, Nature (London) **410**, 277 (2001).

[9] B. Blasius, A. Huppert, and L. Stone, Complex dynamics and phase synchronization in spatially extended ecological systems, Nature (London) **399**, 354 (1999).

[10] C. Volos, I. Kyprianidis, and I. Stouboulos, Synchronization phenomena in coupled nonlinear systems applied in economic cycles, WSEAS Trans. Syst. **11**, 681 (2012).

[11] M. Moussaid, S. Garnier, G. Theraulaz, and D. Helbing, Collective information processing and pattern formation in swarms, flocks, and crowds, Topics Cogn. Sci. **1**, 469 (2009).

[12] L. M. Pecora and T. L. Caroll, Synchronization in Chaotic Systems, Phys. Rev. Lett. **64**, 821 (1990).

[13] G. S. Duane and J. J. Tribbia, Synchronized Chaos in Geophysical Fluid Dynamics, Phys. Rev. Lett. **86**, 4298 (2001).

[14] R. Roy and K. S. Thornburg, Experimental Synchronization of Chaotic Lasers, Phys. Rev. Lett. **72**, 2009 (1994).

[15] G. D. Van Wiggeren, Communication with chaotic lasers, Science **279**, 1198 (1998).

[16] J.-P. Goedgebuer, L. Larger, and H. Porte, Optical Cryptosystem Based on Synchronization of Hyperchaos Generated by a Delayed Feedback Tunable Laser Diode, Phys. Rev. Lett. **80**, 2249 (1998).

[17] S. Boccaletti, J. Kurths, G. Osipov, D. Valladares, and C. Zhou, The synchronization of chaotic systems, Phys. Rep. **366**, 1 (2002).

[18] E.-H. Park, M. A. Zaks, and J. Kurths, Phase synchronization in the forced Lorenz system, Phys. Rev. E **60**, 6627 (1999).

[19] M. A. Zaks, E.-H. Park, M. G. Rosenblum, and J. Kurths, Alternating Locking Ratios in Imperfect Phase Synchronization, Phys. Rev. Lett. **82**, 4228 (1999).

[20] J. A. Blackburn, G. L. Baker, and H. J. T. Smith, Intermittent synchronization of resistively coupled chaotic Josephson junctions, Phys. Rev. B **62**, 5931 (2000).

[21] R. Lifshitz and M. C. Cross, Response of parametrically driven nonlinear coupled oscillators with application to micromechanical and nanomechanical resonator arrays, Phys. Rev. B **67**, 134302 (2003).

[22] A. Pujol-Peré, O. Calvo, M. A. Matias, and J. Kurths, Experimental study of imperfect phase synchronization in the forced Lorenz system, Chaos **13**, 319 (2003).

[23] A. N. Pisarchik, R. Jaimes-Reátegui, and J. H. García-López, Synchronization of coupled bistable chaotic systems: Experimental study, Philos. Trans. R. Soc. A **366**, 459 (2008).

[24] K. V. Volodchenko, V. N. Ivanov, S.-H. Gong, M. Choi, Y.-J. Park, and C.-M. Kim, Phase synchronization in coupled Nd:YAG lasers, Opt. Lett. **26**, 1406 (2001).

[25] L. Midolo, A. Schliesser, and A. Fiore, Nano-opto-electro-mechanical systems, Nat. Nanotechnol. **13**, 11 (2018).

[26] Q. P. Unterreithmeier, E. M. Weig, and J. P. Kotthaus, Universal transduction scheme for nanomechanical systems based on dielectric forces, Nature (London) **458**, 1001 (2009).

[27] A. Eichler, M. del Álamo Ruiz, J. A. Plaza, and A. Bachtold, Strong Coupling between Mechanical Modes in a Nanotube Resonator, Phys. Rev. Lett. **109**, 025503 (2012).

[28] K. Gajo, S. Schüz, and E. M. Weig, Strong 4-mode coupling of nanomechanical string resonators, Appl. Phys. Lett. **111**, 133109 (2017).

[29] H. Okamoto, A. Gourgout, C.-Y. Chang, K. Onomitsu, I. Mahboob, E. Y. Chang, and H. Yamaguchi, Coherent phonon manipulation in coupled mechanical resonators, Nat. Phys. **9**, 480 (2013).

[30] A. Chowdhury, S. Barbay, M. G. Clerc, I. Robert-Philip, and R. Braive, Phase Stochastic Resonance in a Forced Nanoelectromechanical Membrane, Phys. Rev. Lett. **119**, 234101 (2017).

[31] G. Heinrich, M. Ludwig, J. Qian, B. Kubala, and F. Marquardt, Collective Dynamics in Optomechanical Arrays, Phys. Rev. Lett. **107**, 043603 (2011).

[32] C. A. Holmes, C. P. Meaney, and G. J. Milburn, Synchronization of many nanomechanical resonators coupled via a common cavity field, Phys. Rev. E **85**, 066203 (2012).

[33] S.-B. Shim, M. Imboden, and P. Mohanty, Synchronized oscillation in coupled nanomechanical oscillators, Science **316**, 95 (2007).

[34] D. Pu, X. Wei, L. Xu, Z. Jiang, and R. Huan, Synchronization of electrically coupled micromechanical oscillators with a frequency ratio of 3:1, Appl. Phys. Lett. **112**, 013503 (2018).

[35] M. H. Matheny, M. Grau, L. G. Villanueva, R. B. Karabalin, M. C. Cross, and M. L. Roukes, Phase Synchronization of Two Anharmonic Nanomechanical Oscillators, Phys. Rev. Lett. **112**, 014101 (2014).

[36] R. B. Karabalin, M. C. Cross, and M. L. Roukes, Nonlinear dynamics and chaos in two coupled nanomechanical resonators, Phys. Rev. B **79**, 165309 (2009).

[37] S. Houri, M. Asano, H. Yamaguchi, N. Yoshimura, Y. Koike, and L. Minati, Generic Rotating-Frame-Based Approach to Chaos Generation in Nonlinear Micro- and Nanoelectromechanical System Resonators, Phys. Rev. Lett. **125**, 174301 (2020).

[38] J. Ma, C. You, L.-G. Si, H. Xiong, J. Li, X. Yang, and Y. Wu, Formation and manipulation of optomechanical chaos via a bichromatic driving, Phys. Rev. A **90**, 043839 (2014).

[39] J. Larson and M. Horsdal, Photonic Josephson effect, phase transitions, and chaos in optomechanical systems, Phys. Rev. A **84**, 021804(R) (2011).

[40] L. Jin, Y. Guo, X. Ji, and L. Li, Reconfigurable chaos in electro-optomechanical system with negative Duffing resonators, Sci. Rep. **7**, 4822 (2017).

[41] N. Yang, A. Miranowicz, Y.-C. Liu, K. Xia, and F. Nori, Chaotic synchronization of two optical cavity modes in optomechanical systems, Sci. Rep. **9**, 1 (2019).

[42] D. Navarro-Urrios, N. E. Capuj, M. F. Colombano, P. D. García, M. Sledzinska, F. Alzina, A. Griol, A. Martínez, and C. M. Sotomayor-Torres, Nonlinear dynamics and chaos in an optomechanical beam, Nat. Commun. **8**, 14965 (2017).

[43] J. Wu, S.-W. Huang, Y. Huang, H. Zhou, J. Yang, J.-M. Liu, M. Yu, G. Lo, D.-L. Kwong, S. Duan, and C. Wei Wong, Mesoscopic chaos mediated by Drude electron-hole plasma in silicon optomechanical oscillators, Nat. Commun. **8**, 15570 (2017).

[44] K. M. Cuomo, A. V. Oppenheim, and S. H. Strogatz, Synchronization of Lorenz-based chaotic circuits with applications to communications, IEEE Trans. Circuits Syst. II **40**, 626 (1993).

[45] A. Argyris, D. Syvridis, L. Larger, V. Annovazzi-Lodi, P. Colet, I. Fischer, J. García-Ojalvo, C. R. Mirasso, L. Pesquera, and K. A. Shore, Chaos-based communications at high bit rates using commercial fibre-optic links, Nature (London) **438**, 343 (2005).

[46] V. Annovazzi-Lodi, S. Donati, and A. Scire, Synchronization of chaotic injected-laser systems and its application to optical cryptography, IEEE J. Quantum Electron. **32**, 953 (1996).

[47] C. R. Mirasso, P. Colet, and P. Garcia-Fernandez, Synchronization of chaotic semiconductor lasers: Application to encoded communications, IEEE Photonics Technol. Lett. **8**, 299 (1996).

[48] M. Sciamanna and K. Shore, Physics and applications of laser diode chaos, Nat. Photonics **9**, 151 (2015).

[49] A. Roy and M. Devoret, Introduction to parametric amplification of quantum signals with Josephson circuits, C. R. Phys. **17**, 740 (2016).

[50] H. C. S. Hsuan, R. C. Ajmera, and K. E. Lonngren, The nonlinear effect of altering the zeroth order density distribution of a plasma, Appl. Phys. Lett. **11**, 277 (1967).

[51] M. G. Clerc, S. Coulibaly, M. A. Ferré, and R. G. Rojas, Chimera states in a Duffing oscillators chain coupled to nearest neighbors, Chaos **28**, 083126 (2018).

[52] T. Antoni, A. G. Kuhn, T. Briant, P.-F. Cohadon, A. Heidmann, R. Braive, A. Beveratos, I. Abram, L. L. Gratiet, I. Sagnes, and I. Robert-Philip, Deformable two-dimensional photonic crystal slab for cavity optomechanics, Opt. Lett. **36**, 3434 (2011).

[53] A. Chowdhury, I. Yeo, V. Tsvirkun, F. Raineri, G. Beaudoin, I. Sagnes, R. Raj, I. Robert-Philip, and R. Braive, Superharmonic resonances in a two-dimensional non-linear photonic-crystal nano-electro-mechanical oscillator, Appl. Phys. Lett. **108**, 163102 (2016).

[54] Y. S. Joe, A. M. Satanin, and C. S. Kim, Classical analogy of Fano resonances, Phys. Scr. **74**, 259 (2006).

[55] M. F. Limonov, M. V. Rybin, A. N. Poddubny, and Y. S. Kivshar, Fano resonances in photonics, Nat. Photonics **11**, 543 (2017).

[56] S. Stassi, A. Chiadò, G. Calafiore, G. Palmara, S. Cabrini, and C. Ricciardi, Experimental evidence of Fano resonances in nanomechanical resonators, Sci. Rep. **7**, 1065 (2017).

[57] J. F. Rhoads, S. W. Shaw, and K. L. Turner, Nonlinear dynamics and its applications in micro- and nanoresonators, J. Dyn. Syst., Meas., Control **132**, 034001 (2010).

[58] A. Chowdhury, M. G. Clerc, S. Barbay, I. Robert-Philip, and R. Braive, Weak signal enhancement by nonlinear resonance control in a forced nano-electromechanical resonator, Nat. Commun. **11**, 2400 (2020).

[59] S. Zanotto, Weak coupling, strong coupling, critical coupling and Fano resonances: A unifying vision, in *Fano Resonances in Optics and Microwaves: Physics and Applications*, edited by E. Kamenetskii, A. Sadreev, and A. Miroshnichenko (Springer International Publishing, Cham, 2018), pp. 551–570.

[60] R. Hegger, H. Kantz, and T. Schreiber, Practical implementation of nonlinear time series methods: The TISEAN package, Chaos **9**, 413 (1999).

[61] M. T. Rosenstein, J. J. Collins, and C. J. D. Luca, A practical method for calculating largest Lyapunov exponents from small data sets, Physica D **65**, 117 (1993).

[62] C. Lee, T. Yoon, and S. Shin, Period doubling and chaos in a directly modulated laser diode, Appl. Phys. Lett. **46**, 95 (1985).

[63] J. Miles, Chaotic motion of a weakly nonlinear, modulated oscillator, Proc. Natl. Acad. Sci. USA **81**, 3919 (1984).

[64] R. Meucci, S. Euzzor, E. Pugliese, S. Zambrano, M. R. Gallas, and J. A. C. Gallas, Optimal Phase-Control Strategy for Damped-Driven Duffing Oscillators, Phys. Rev. Lett. **116**, 044101 (2016).

[65] P. J. Martínez, S. Euzzor, J. A. Gallas, R. Meucci, and R. Chacón, Identification of minimal parameters for optimal suppression of chaos in dissipative driven systems, Sci. Rep. **7**, 1 (2017).

[66] P. J. Martínez, S. Euzzor, R. Meucci, and R. Chacón, Suppression of chaos by incommensurate excitations: Theory and experimental confirmations, Commun. Nonlinear Sci **83**, 105137 (2020).

[67] D. Cadeddu, F. R. Braakman, G. Tütüncüoglu, F. Matteini, D. Rüffer, A. Fontcuberta i Morral, and M. Poggio, Time-resolved nonlinear coupling between orthogonal flexural modes of a pristine gaas nanowire, Nano Lett. **16**, 926 (2016).

[68] L. Mercier de Lépinay, B. Pigeau, B. Besga, and O. Arcizet, Eigenmode orthogonality breaking and anomalous dynamics in multimode nano-optomechanical systems under non-reciprocal coupling, Nat. Commun. **9**, 1401 (2018).

[69] J. Rieger, T. Faust, M. J. Seitner, J. P. Kotthaus, and E. M. Weig, Frequency and Q factor control of nanomechanical resonators, Appl. Phys. Lett. **101**, 103110 (2012).